2026 IEEE 39th International Conference on Micro Electro Mechanical Systems (MEMS) | 979-8-3315-7251-8/26/$31.00 ©2026 IEEE | DOI: 10.1109/MEMS64181.2026.11419515

MACHINE LEARNING ENABLED MEMS RECONFIGURABLE INTELLIGENT SURFACE FOR TERAHERTZ BEAM STEERING AND WIRELESS COMMUNICATION

Yinpeng Wang[1], Qiqi Dai[1], Cheng Xu[1], Dongxiao Li[1], Zhihao Ren[1], Luwei Wang[1], Nanhan Liu[2], Chong Pei Ho[2], Prakash Pitchappa[2], and Chengkuo Lee[1,]*

[1]National University of Singapore, SINGAPORE and

[2]Agency for Science, Technology and Research, SINGAPORE

ABSTRACT

This work presents a CMOS-compatible MEMS-based terahertz reconfigurable intelligent surface (THz RIS) designed through a machine-learning-assisted framework. Leveraging the Kolmogorov–Arnold Network (KAN) as an efficient surrogate model, we achieve rapid and accurate prediction of transmission spectra, enabling optimized design of deformable L-shaped MEMS meta-atoms. The fabricated RIS demonstrates broadband (0.3–0.8 THz), ultra-wide-angle (±60°) beam steering with high diffraction contrast, together with programmable amplitude/phase modulation for spatial–temporal THz coding. We further realize directional transmission of text and images with high fidelity, highlighting the platform's potential for future high-data-rate and adaptive THz communication systems.

KEYWORDS

Terahertz Reconfigurable Intelligent Surface; MEMS Metasurface; Machine-Learning-Assisted Design.

INTRODUCTION

Terahertz (THz) reconfigurable intelligent surfaces (RIS) have emerged as a promising paradigm for dynamic wavefront control in next-generation wireless systems. By integrating active elements into subwavelength meta-atoms, THz RIS can provide programmable control over amplitude and phase across large apertures, enabling beam steering, spatial multiplexing, and adaptive propagation tailoring in the 0.1–10 THz band. These capabilities are particularly attractive for high-data-rate communications [1], imaging [2], and sensing [3-14], where compact form factor, low power consumption, and compatibility with integrated platforms are essential.

Current THz RIS implementations employ a variety of tuning mechanisms, including semiconductor [15], or liquid-crystal [16] based modulation, phase-change-material [17] based modulation, optically driven control [18], and mechanically reconfigurable structures [19-22]. While these approaches have demonstrated beam steering and multifunctional responses, they generally suffer from trade-offs in modulation depth, speed, stability, scalability, or system complexity. In particular, MEMS-based metasurface offer large tuning ranges and CMOS compatibility, but most reported devices remain at the proof-of-concept level, with limited wavefront engineering, narrow steering ranges, and design workflows that rely on computationally expensive full-wave simulations and manual parameter sweeps.

Recently, deep learning technology has shone brightly in the field of electromagnetic simulation [23-26]. In this work, we develop a CMOS-compatible MEMS-based THz RIS that is designed through a machine-learning-assisted framework (Figure 1). Using a Kolmogorov–Arnold Network (KAN) surrogate model [27], we efficiently map deformable L-shaped MEMS geometries to complex transmission spectra, achieving orders-of-magnitude acceleration and higher accuracy compared with conventional neural networks and FDTD simulations. The optimized electro-thermally actuated RIS realizes π-phase switching at 0.6 THz, broadband (0.3–0.8 THz) and ultra-wide-angle (−60° to 60°) beam steering, and programmable spatial–temporal coding for directional THz data transmission of text and images, providing a scalable route toward intelligent THz front ends for future 6G and beyond systems.

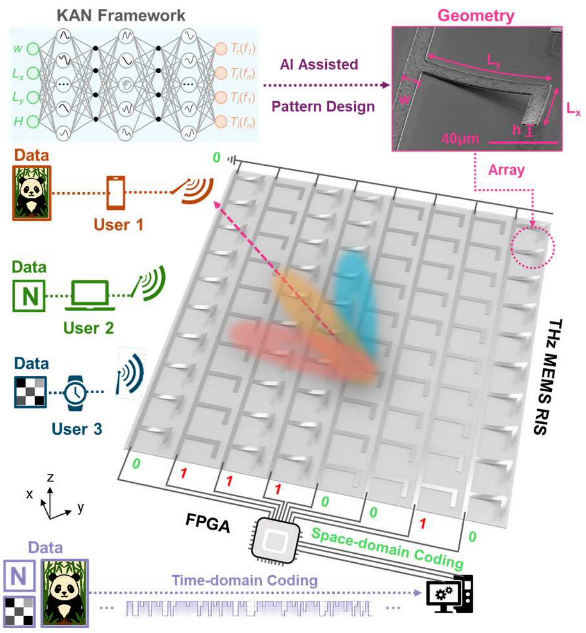

Figure 1: System framework for MEMS terahertz reconfigurable intelligent surface based on deep learning assisted design.

RESULTS AND DISCUSSIONS

Concept of MEMS-based THz RIS

The proposed MEMS-based THz reconfigurable intelligent surface (RIS) consists of an electro-thermally tunable resonator array integrated with a broadband continuous-wave THz source, transmitting and receiving antennas, and an FPGA controller. The 125 × 100-element array is column-addressed through shared bias lines, so that all unit cells in a given column experience the same complex transmission coefficient. By programming binary or multi-level ON/OFF states along the array, space-domain coding sequences steer the transmitted beam toward desired angles, while time-domain coding modulates the THz carrier with user data, enabling directional and multiplexed communication links.

Each unit cell is implemented on a high-resistivity silicon substrate and comprises unreleased Mo–Al bimorph lines and a released L-shaped cantilever. The Mo/Al thickness combination defines an initial out-of-plane displacement, and Joule heating induced by the bias current generates differential thermal expansion, which bends the cantilever toward or away from the substrate. This mechanical reconfiguration produces large and controllable changes in the THz transmission amplitude and phase at the unit-cell level, forming the physical basis for broadband beam steering and programmable spatial–temporal coding across the entire RIS aperture.

Geometric Parameter Design via KAN

To efficiently explore the high-dimensional design space of deformable MEMS meta-atoms, we employ a Kolmogorov–Arnold Network (KAN) as a surrogate model that maps geometric parameters to complex transmission spectra. The input vector $G = (w, L_x, L_y, H)$ encodes the cantilever width, arm lengths, and tip–substrate distance, while the output is a 100-dimensional vector Trepresenting the complex transmission coefficients sampled from 0.3–0.8 THz. The network is trained on 4,000 geometry–spectrum pairs generated by Lumerical FDTD, with an equal split between training and test sets. Compared with a multilayer perception of similar complexity, the KAN converges faster and yields mean-squared errors about two orders of magnitude lower, while predicting spectra more than four orders of magnitude faster than full-wave simulations and maintaining excellent agreement in both amplitude and phase.

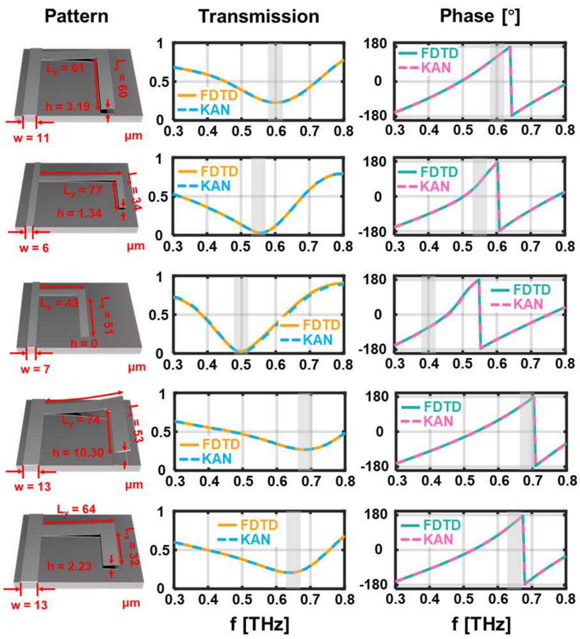

Figure 2: Samples to demonstrate performance of the proposed KAN in predicting the transmission and phase.

The trained KAN is then used to optimize the geometric parameters for a target operating frequency f_0 = 0.6 THz. We scan w, L_x, and L_y while considering an ON state with H = 0 μm and an OFF state defined by a tip deflection angle of 8.5°. For each candidate geometry, the KAN-predicted transmission amplitudes A_1, A_0 and phase difference φ are used to evaluate the first- to zeroth-order diffraction power ratio η. Figure 2 displays several samples to demonstrate predicting performance of KAN. We can find that KAN coincidences well with FDTD simulations. The optimal design identified by this search yields η ≈ 38 dB near $w \approx$ 9.75 μm, $L_x \approx$ 30.35 μm, and $L_y \approx$ 74.55 μm; for fabrication compatibility we adopt rounded values $w \approx$ 10 μm, $L_x \approx$ 30 μm, and $L_y \approx$ 75 μm, which still provide high diffraction contrast for efficient beam steering.

Unit Simulation and Experimental Validation

Using optimized geometric parameters, we first performed full-wave simulations of a single L-shaped MEMS meta-atom under normal incident, y-polarized THz illumination. The simulated and measured transmission spectra in Figure 3**a** shows that, as the cantilever tip height decreases from the released OFF state to the fully contacted ON state, the resonance peaks by about 0.3 THz and the transmission phase undergoes a nearly 180° change around 0.6 THz, fulfilling the requirement for binary phase coding. Experimental transmission spectra measured with a THz time-domain spectroscopy setup under different bias currents is displayed in Figure 3**b**, exhibiting similar resonance shifting and amplitude evolution and agree well with the KAN-predicted responses in the designed frequency band, confirming the accuracy of the surrogate-based design. Figure 3**c** presents the simulated nearfield at ON/OFF state, while Figure 3**d** elaborates the optical and SEM image.

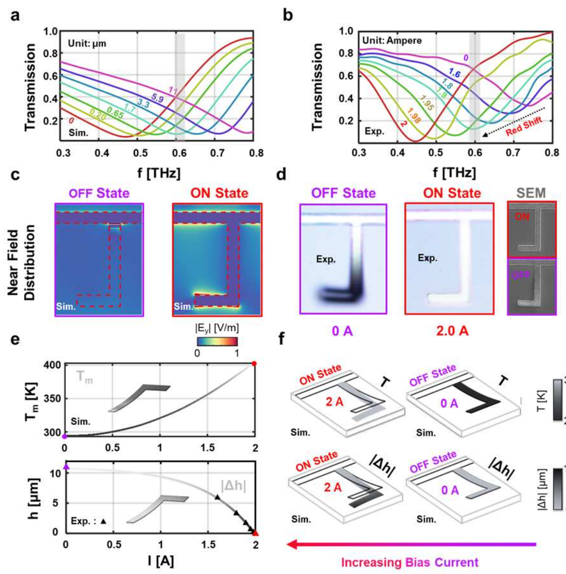

Figure 3: Simulation and testing results of RIS unit. **a** *and* **b** *Simulated/measured transmission of different bending heights,* **c** *Simulated near field at ON/OFF state,* **d** *Optical and SEM of MEMS unit at ON/OFF state,* **e** *and* **f** *Simulated and measured formation under different bias.*

To elucidate the electromechanical behavior, we modeled the coupled electro–thermal–mechanical response of the bimetallic cantilever in COMSOL. Joule heating raises the device temperature approximately quadratically with current, and the mismatch in thermal expansion between Mo and Al induces progressive out-of-plane bending. The simulated dependence of maximum temperature and tip displacement on current in Figure 3**e** is in close agreement with confocal microscopy measurements. Temperature field and deformation maps in Figure 3**f** further reveal that increasing the current from 0 A to 2 A elevates the peak temperature from room temperature to about 390 K and increases the tip displacement from 0 to approximately 11 μm. Optical micrographs taken at representative bias points show the cantilever gradually approaching and finally contacting the substrate, providing direct visual confirmation of the simulated actuation process and its role in modulating the unit-cell transmission response.

Reconfigurable THz Beam Steering

To evaluate the beam-steering capability of the proposed metasurface, we implement one-dimensional spatial coding along the column direction of the 125 × 100 MEMS array. Each column is programmed into either the ON or OFF state, corresponding to two complex transmission coefficients with approximately π phase difference at the design frequency. By arranging these states into periodic 0/1 sequences, we synthesize effective phase gratings with different coding periods. As shown in Figure 4a, four metasurface with periods of 800, 1000, 1200, and 1600 μm are realized in our prototype, in which half of the elements are tunable and the remaining ones are fixed in the ON state, enabling reconfigurable control of diffraction orders through simple column-wise current programming.

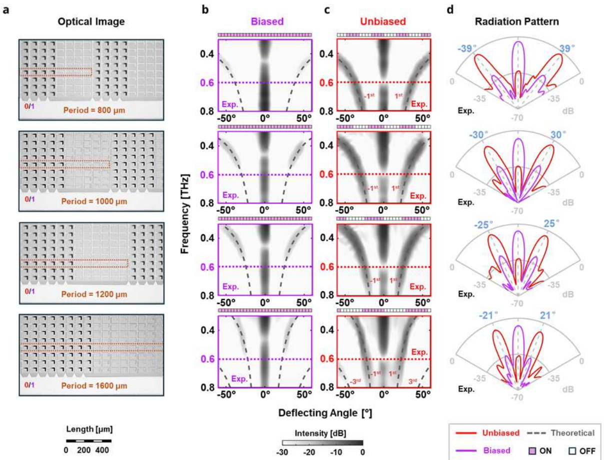

Figure 4: Measured results for THz beam steering. **a** *Optical micrographs of chips with different coding,* **b** *and* **c** *Measured receiving spectrum at ON/OFF states,* **d** *Measured radiation pattern at 0.6 THz.*

Far-field transmission measurements are performed using an angle-resolved THz time-domain spectroscopy setup, recording the received power from −60° to 60° over 0.3–0.8 THz. When all tunable elements are biased to the ON state, the transmitted energy is primarily concentrated in the zeroth diffraction order (Figure 4**b**). When the bias is removed and the tunable columns switch to the OFF state, the dominant energy is redistributed into the ±1st orders (Figure 4**c**), yielding pronounced beam deflection across the entire operating band. The measured steering angles closely follow the theoretical predictions set by the coding period, and a directional power contrast of approximately 20 dB between the target and zeroth-order beams is obtained near 0.6 THz (Figure 4**d**), confirming efficient and broadband reconfigurable THz beam steering using the MEMS-based RIS platform.

Programmable THz Information Transmission

For directional information transfer, we configure the MEMS-based RIS in a point-to-point link comprising a broadband THz source, transmitting and receiving antennas, and an FPGA-controlled current driver. Figure 5**a** and 5**b** display the conceptual and physical diagrams of the transmission system. The directional response is characterized by monitoring the transmission coefficient toward 40°, where increasing the bias current from 0 A to 2 A reduces the peak transmission at 0.59 THz from 0.42 to 0.065, providing sufficient modulation depth for both binary and multi-level encoding. A one-bit scheme with a single amplitude threshold distinguishes ON/OFF states, while a two-bit scheme with three thresholds defines four discrete transmission levels (Figure 5**c**).

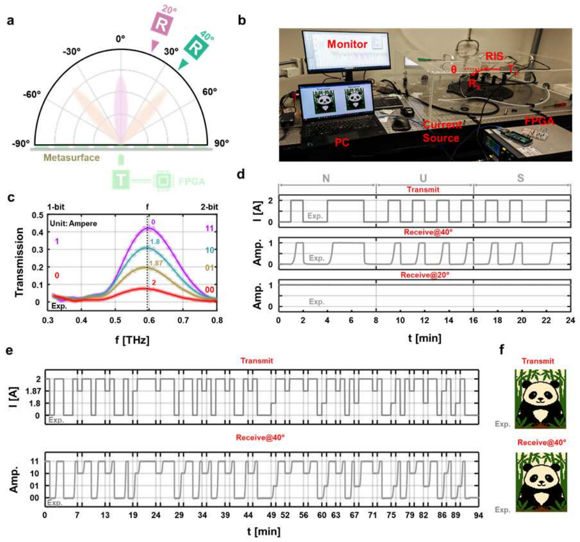

Figure 5: Testing results of programmable THz transmission system. **a** *Concept diagram of the system,* **b** *Photographs of the measurement system,* **c** *Illustration for one/two-bit coding,* **d** *Time domain sequence of text transmission via ASCII encoding,* **e** *Time domain sequence of color image transmission experiment,* **f** *Transmitted and received color images.*

Using this spatial–temporal coding platform, we experimentally demonstrate two representative transmission scenarios: ASCII-encoded text and 128 × 86 four-color images. For the text experiment in Figure 5**d**, the string "NUS" is mapped to binary sequences and directed to 40°, where the received waveform accurately reproduces the transmitted data, while a non-target direction (20°) carries no recoverable information. For color images, a singular value decomposition–based compression encodes the dominant singular vectors into temporal current sequences (Figure 5**e**), yielding a reconstructed image that is visually indistinguishable from the original and achieves a peak signal-to-noise ratio exceeding 34 dB (Figure 5**f**). These results verify that the MEMS-based RIS supports high-fidelity, directional THz communications with programmable multi-level modulation.

CONCLUSIONS

In summary, we have demonstrated a CMOS-compatible MEMS-based THz reconfigurable intelligent surface designed through a Kolmogorov–Arnold Network assisted framework. The KAN surrogate enables rapid and accurate prediction of complex transmission spectra, greatly accelerating geometry optimization beyond conventional full-wave simulations. The fabricated RIS achieves π-phase switching at 0.6 THz, broadband (0.3–0.8 THz) and ultra-wide-angle (±60°) beam steering, and programmable spatial–temporal coding for directional transmission of text and images with high fidelity. These results highlight a scalable and versatile platform for intelligent THz front-ends, and pave the way toward faster electrostatically actuated devices for future 6G communication systems.

ACKNOWLEDGEMENTS

This work was supported by A*STAR MTC Programmatic Funds under grant no. M22L1b0110, National Centre for Advanced Integrated Photonics under grant NRF-MSG-2023-0002, Frontier CRP under grant NRF-F-CRP-2024-0006, and Microelectronics Seed Grant Funding under grant A-8003551-00-00.

REFERENCES

[1] M. Wei, H. Zhao, V. Galdi, L. Li, and T. J. Cui, "Metasurface-enabled smart wireless attacks at the physical layer," *Nat. Electron.*, vol. 6, no. 8, pp. 610–618, Aug. 2023.

[2] J. Chen, S.-X. Huang, K. F. Chan, G.-B. Wu, and C. H. Chan, "3D-printed aberration-free terahertz metalens for ultra-broadband achromatic super-resolution wide-angle imaging with high numerical aperture," *Nat. Commun.*, vol. 16, no. 1, pp. 1–9, Jan. 2025.

[3] S. Karmakar, A. Kludze, R. Chandra, and Y. Ghasempour, "Sub-terahertz metamaterial stickers for non-invasive fruit ripeness sensing," *Nat. Food*, vol. 6, no. 1, pp. 97–104, Jan. 2025.

[4] H. Zhou *et al.*, "Surface plasmons-phonons for mid-infrared hyperspectral imaging," *Sci. Adv.*, vol. 10, no. 22, May 2024.

[5] D. Li, H. Zhou, Z. Ren, C. Xu, and C. Lee, "Tailoring light–matter interactions in overcoupled resonator for biomolecule recognition and detection," *Nano-Micro Lett.*, vol. 17, no. 1, Sep. 2024.

[6] J. Wei *et al.*, "Geometric filterless photodetectors for mid-infrared spin light," *Nat. Photonics*, vol. 17, Dec. 2022.

[7] C. Xu *et al.*, "Expanding chiral metamaterials for retrieving fingerprints via vibrational circular dichroism," *Light Sci. Appl.*, vol. 12, no. 1, Jun. 2023.

[8] H. Zhou *et al.*, "Dynamic construction of refractive index-dependent vibrations using surface plasmon-phonon polaritons," *Nat. Commun.*, vol. 14, no. 1, Nov. 2023.

[9] Z. Ren, Z. Zhang, J. Wei, B. Dong, and C. Lee, "Wavelength-multiplexed hook nanoantennas for machine learning enabled mid-infrared spectroscopy," *Nat. Commun.*, vol. 13, no. 1, Jul. 2022.

[10] H. Zhou, D. Li, and C. Lee, "Technology landscape review of in-sensor photonic intelligence: From optical sensors to smart devices," *AI Sens.*, vol. 1, no. 1, p. 5, Jul. 2025

[11] T. Leng, L. Li, and C. Lee, "Journal editorial: Welcome to the new era of AI-enabled sensing," *AI Sens.*, vol. 1, no. 1, p. 1, Feb. 2025.

[12] M. Xiao, A. Xu, Z. Sui, W. Zhang, H. Liu, and C. Lee, "Multifunctional MEMS, NEMS, micro/nano-structures enabled by piezoelectric and ferroelectric effects," *Nanoscale Horiz.*, vol. 10, no. 11, pp. 2744–2771, 2025.

[13] D. Li, H. Zhou, Z. Ren, and C. Lee, "Advances in MEMS, optical MEMS, and nanophotonics technologies for volatile organic compound detection and applications," *Small Sci.*, vol. 5, no. 4, Jan. 2025.

[14] X. Guo, Z. Zhang, Z. Ren, D. Li, C. Xu, L. Wang, et al., "Advances in intelligent nano-micro-scale sensors and actuators: Moving toward self-sustained edge AI microsystems," *Adv. Mater.*, Sep. 2025.

[15] S. Venkatesh, X. Lu, H. Saeidi, and K. Sengupta, "A high-speed programmable and scalable terahertz holographic metasurface based on tiled CMOS chips," *Nat. Electron.*, vol. 3, no. 12, pp. 785–793, Dec. 2020.

[16] W. Li *et al.*, "Modulo-addition operation enables terahertz programmable metasurface for high-resolution two-dimensional beam steering," *Sci. Adv.*, vol. 9, no. 42, Oct. 2023.

[17] B. Chen *et al.*, "Electrically addressable integrated intelligent terahertz metasurface," *Sci. Adv.*, vol. 8, no. 41, Oct. 2022.

[18] L. Cong *et al.*, "All-optical active THz metasurfaces for ultrafast polarization switching and dynamic beam splitting," *Light Sci. Appl.*, vol. 7, no. 1, Jul. 2018.

[19] W. Liu, S. Xu, and C. Lee, "Ultracompact on-chip spectral shaping using pixelated nano-opto-electro-mechanical gratings," *Science*, vol. 389, no. 6762, pp. 806–810, Aug. 2025.

[20] M. Manjappa *et al.*, "Reconfigurable MEMS Fano metasurfaces with multiple-input–output states for logic operations at terahertz frequencies," *Nat. Commun.*, vol. 9, no. 1, Oct. 2018.

[21] P. Pitchappa, C. P. Ho, L. Dhakar, and C. Lee, "Microelectromechanically reconfigurable interpixelated metamaterial for independent tuning of multiple resonances at terahertz spectral region," *Optica*, vol. 2, no. 6, p. 571, Jun. 2015.

[22] L. Cong, P. Pitchappa, C. Lee, and R. Singh, "Active phase transition via loss engineering in a terahertz MEMS metamaterial," *Adv. Mater.*, vol. 29, no. 26, May 2017.

[23] S. Qi *et al.*, "Two-dimensional electromagnetic solver based on deep learning technique," *IEEE J. Multiscale Multiphys. Comput. Tech.*, vol. 5, pp. 83–88, 2020.

[24] Y. Li *et al.*, "Predicting scattering from complex nano-structures via deep learning," *IEEE Access*, vol. 8, pp. 139983–139993, 2020.

[25] Y. Wang and S. Zhang, "Multi-receptive-field physics-informed neural network for complex electromagnetic media," *Opt. Mater. Express*, vol. 14, no. 11, p. 2740, Oct. 2024.

[26] Y. Wang and Q. Ren, Deep Learning-Based Forward Modeling and Inversion Techniques for Computational Physics Problems, 1st ed. Boca Raton, FL, USA: CRC Press, 2023, pp. 1–34.

[27] Z. Liu et al., "KAN: Kolmogorov-Arnold Networks," in *Proc. Int. Conf. Learn. Represent.* (ICLR), Singapore, Apr. 2025. [Online].

CONTACT

*Chengkuo Lee: elelc@nus.edu.sg